Designing Ring-Like Flexible Colloidal Structures

Houston, Yahel

Designing Ring-Like Flexible Colloidal Structures

THESIS

submitted in partial fulfillment of the
requirements for the degree of

MASTER OF SCIENCE
in
PHYSICS

Author :	Yahel Houston
Student ID :	s2547651
Supervisor :	Daniela Kraft
Second corrector :	Martin van Hecke

Leiden, The Netherlands, December 16, 2021

Designing Ring-Like Flexible Colloidal Structures

Yahel Houston

Huygens-Kamerlingh Onnes Laboratorium, Universiteit Leiden
P.O. Box 9500, 2300 RA Leiden, The Netherlands

December 16, 2021

Abstract

Colloidal molecules are a recent development in the field of physics, with specific tailoring towards certain properties such as directional bonding and flexibility. The advantage of using colloids is that they provide an excellent starting point to understanding and emulating the dynamics of their molecular counterpart. These parallels can be drawn since colloidal molecules are still sensitive to thermal fluctuations and move much slower than molecules, meaning direct observations can be made. In this thesis, we explore building a ring-like structure out of spherical and cubic colloid supported lipid bilayers (CSLB). The unique aspect of this project, is that in this combined use there is both directional bonding, flexibility and constrained internal motion. The overarching aim is to understand the conformations of a 8 particle ring formed from alternating sphere and cube colloids, with the cubes being on the corners. To do this, we analyse individual angles to look at the conformations as well the structural changes, done using mode analysis

Contents

Chapter 1

Introduction

Colloids, being a dispersion of one microscopic particle in another substance, pop up everywhere in our daily lives, whether it is the milk that we drink, or the paint we look at on our walls. Colloids come in many shapes and forms, such as emulsions (liquid in a liquid), gels (liquid in a solid) or sols (solid in a liquid). There are many applications to the studies of sols, for example in industrial coatings [1] to micro-nanorobots [2]. However, one of the most relevant of colloids to this thesis is using colloids, or more specifically colloidal molecules as a model study system [3]. This project is particularly relevant since it uses flexible colloidal molecules with constraints, relevant to creating joints for nano-robots or understanding the dynamics of a constrained molecule. Constraints here refer to a structure or bond that has limited movement possible in a certain direction.

Because of their small size and fast movements, the individual dynamics of atoms, or atoms within a molecule are inherently hard to study. Direct, *in-situ* observations of conformational changes of molecules are difficult, since they require single-molecule imaging techniques with high spatial and temporal resolution. As such, model systems are often used as counterparts to study dynamics or conformational changes, an example of such is being the study of pseudorotation (continuous conversion between conformations) of alkanes [4]. The pseudorotation of a molecule such as cyclopentane has only been observed indirectly [5] and represents a behaviour that is hard to access by direct measurement of the molecule. Instead, colloids can be used to act as model atoms, such that easier measurements can be taken. In the paper by Swinkels [4], colloids have directional bonding, meaning they can be designed to take the same shapes as molecules such as cyclopentane. The study not only shows a method to design colloidal molecule to make a direct representation of a molecule,

Version of December 16, 2021– Created December 16, 2021 - 22:24

but it is also able to directly observe the pseudorotation of the colloidal counterpart. Whilst directional bonding is a more recent development in the field of colloidal science, the combination of this and the fact that colloids are easy to image and still are sensitive to thermal fluctuations make them excellent systems to understand molecular dynamics.

Rigid colloidal molecular structures have been prepared and studied extensively [6] and it is only recently that flexiblity was introduced in colloidal structures. This enables the experimental study of the dynamics of structures that posses flexibility. The work conducted by Verweij et al. [7] allowed for direct observations of diffusive shape-changing objects, similar to systems that may be inaccessible to direct observations like biopolymers. This study looked at the effect of segmental flexibility of a trimer, a colloidal molecule consisting of three spheres. The study reveals that flexibilty has an effect on the Brownian motion on short and long timescales, with the fact that not only does rotation affect the diffusion, but also the conformational changes. Biological molecules such as enzymes exhibit segmental flexibility which can affect their biological function [8], therefore studies such as this aide in the understanding of the dynamics of these systems.

This paper was built upon the work of Chakraborty et. al [9], where colloid supported lipid bilayers (CSLBs) are used to build the colloidal molecules, explained in the next paragraph. Chakraborty et al. demonstrated the motion of colloidal joints built with different colloid shapes and the ability of joints like this to have tunable flexibility. The flexibility can be tuned in different ways, either by the size of the colloids, or the density of the linker DNA (see below). A sphere-sphere joint-like motion was demonstrated to rotate around 360°, whereas a sphere-cube joint has a slider-like motion. Slider-like motion is a result of the spheres only being able to diffuse on a face of a cube, rather than over the edge of a cube. This indicates a type of conformational restriction, where the direction and position of a colloid can be restricted. Studies like these both discussed can be extended to understand a flexible and constrained molecule, relevant to ring polymers or folding genomes [10]. Here, direct access to observations of the molecules is still hard, therefore designing colloidal molecules to represent these systems should help in understanding their dynamics.

The experiments conducted in this thesis are a culmination of these two ideas, namely creating a ring-like flexible colloid structure and using cube-sphere joints to introduce conformational constraints. To achieve this, similar methods are used to Verweij [7] and Chakraborty [9], which utilises colloid supported lipid bilayers (CSLBs) to act as building block for designing bigger structures. CSLBs are colloids that are coated in a lipid

bilayer, which in turn can be functionalised with DNA linkers that have sticky ends that anchor to the lipid bilayer. Sticky ends are single stranded, but complementary to one another, meaning a joint can be formed between two strands and therefore two differently functionalised particles. The lipid bilayer on the surface of the particles is mobile, meaning the linker DNA is able to diffuse over the surface of the particle. In bonding, it is not only one, but many linkers that attach to each other, forming a bonding "patch". One way to tune the flexibility, is to change the density of the linkers on the surface, effectively reducing or increasing the number of DNA linkers involved in bonding. Conformational restraint are introduced by use of slider joints [9], created by using a cube-sphere bond. Here, it is expected that due to the restricted motion of the spheres along the face of the cube, there should also be restrictions on the conformations as a whole. Much like the other studies presented here, this project uses optical tweezers instead of self assembly to form the structures. This has the great advantage that structures can be built precisely and immediately, rather than having to wait for a structure to form and having a low yield of the desired structure as is done with self assembly methods [11].

The aim of this project is to investigate the conformational constraints and shape changes of a 3×3 ring-like structure made out of alternating sphere and cube colloids. This is done in two ways, the first analysis looks at how the conformational constraints affect the system, i.e what is the probability that a certain angle occurs. In this analysis, the structure is said to have two main angles, a corner angle and a side angle. The corner angles are where there is a sphere-cube-sphere joint, where the joint initially is at a 90° angle, the side angle is where there is a cube-sphere-cube joint which exists at a roughly 180° angle. The second analysis looks at the structural changes via mode analysis, this being what are the most likely ways that the structure changes shape.

The thesis will proceed as follows; First, the process of preparing the samples is described, with discussions on how to create the structures and how the data was acquired and analyzed. Later, we look at some of the system's theoretical predictions followed by the primary outcomes of the studies. Finally, conclusions are drawn from results and ideas and information on what can be improved in the experimental setup are given.

Version of December 16, 2021– Created December 16, 2021 - 22:24

Chapter 2

Methods

2.1 Sample Preparation

In order to create the intended structure, first, the individual components need to be prepared. This can be summarised by the following steps; dilute and wash the sphere/ cube colloids, prepare the small unilamellar vesicles (SUVs), coat the particles with the SUVs (resulting in a lipid bilayer), hybridise the DNA and finally add the DNA to the coated particles. Much of the following are similar procedures to those in [7], [9], an overview of this procedure is shown in Fig 2.1.

2.1.1 Materials

Listed below are the materials needed for the functionalisation of the sphere and cubic particles. Silica spheres (Microparticles GMBH, $2.12 \pm 0.06 \mu$m, 5% w/v, stored at 4°C). Cubic particles, silica with hematite core (2.3μm), synthesised by Y. Shelke [13]. Water used in these experiments is water purified by a MilliQ. machine. All lipids are obtained from Avanti Polar Lipids, Inc at >99% purity, stored in chloroform (25g/L DOPC, 10g/L DOPE-PEG2000, 1g/L for DOPE-Rhodamine and Cholesterol- TopFluor): 1,2 dioleoyl-sn-glycero-3-phosphocholine (DOPC), 1,2-dioleoyl -sn-glycero-3 -phosphoethanolamine -N- [methoxy(polyethylene glycol)-2000] (DOPE-PEG2000), 1,2-dioleoyl-sn-glycero- 3-phosphoethanolamine-N-(lissamine rhodamine B sulfonyl) (DOPE-Rhodamine), 23 - (dipyrromethene boron difluoride)-24-norcholesterol (Cholesterol- TopFluor). To prepare the buffer the following chemicals are needed: 4-(2-hydroxyethyl) -1- piperazineethanesulfonic acid (HEPES, Carl Roth, >99.5% purity), sodium chloride (NaCl, Acros Organics, Extra pure), NaOH to adjust pH. Two types of buffer

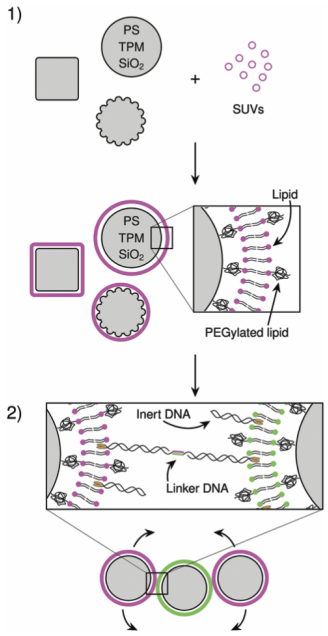

Figure 2.1: *An extract from [12] showing the formation of CSLBs. Step 1) shows that when you add colloidal particles to SUVs, the SUVs are able to form a lipid bilayer over the surface of the particle. Step 2) is the functionalisation of the CSLBs with linker DNA. With complementary strands, this allows for two particles to attach to each other with a flexible link.*

are used in these experiments; HEPES buffer - 1 was made with 50 mM NaCl, 10 mM HEPES, pH 7.4, HEPES buffer - 2 was made with 200 mM NaCl, 10 mM HEPES, pH 7.4. DNA strands used are shown in Table 2.1. The chemicals used in the poly acrylamide (PAA) coated slides are as follows: 3-(Trimethoxysilyl)propyl methacrylate (TPM, Sigma Aldrich, 98% purity), 40% w/w acrylamide in water (Acros Organics), bis-acrylamide (Acros Organics), N,N,N′,N′-Tetramethylethylenediamine (TEMED) · ammonium persulfate(APS, Acros Organics, 98% purity, powder form), Acetic acid (Sigma Aldrich, 99.8% purity), ethanol (Honeywell, 99.8% purity), acetone (VWR), MilliQ water, potassium hydroxide (KOH, 3M, Fisher Chemicals).

2.1.2 Preparation of Spheres/Cubes

In the experiments presented, spherical and cubic silica particles are used. 5μL of the spherical particles are diluted to 0.05% w/v by adding 495μL MilliQ water. The hematite core in the cubic particles is removed, both

because they could not be trapped by the optical tweezers and the possibility of dipole-dipole interactions between cubes in the structure. The concentration of the cubes (at first unknown) is calculated as follows; take a known volume of the solution, then dry this volume of solution such that only the particles remain. The weight by volume of the particles can then be calculated by measuring the mass of the particles divided by the pre-known volume. This solution is also diluted down to 0.05% w/v by taking 5 μL and adding 495 μL of MilliQ water. Once the particles are prepared with the desired concentration, they are washed once to remove any potential contaminates. This is done by placing the particles in a centrifuge for 2 min at 800rpm so that the particles end up in the bottom of the vial, the volume of liquid present is taken out and then refilled with water.

2.1.3 Preparation of Small Unilamellar Vesicles (SUVs)

To prepare small unilamellar vesicles, 77 μL of 25 g/L DOPC, 7.34 μL of 10 g/L DOPE PEG-2000 and 4 μL of 1 g/L DOPE-Rhodamine or TopFluor-Cholesterol (in chloroform) is added to either vial. The solution is placed in a vacuum desiccator for 2+ hours to remove the chloroform. Once fully dried out, 1 mL of filtered HEPES buffer-1 is added, which is then tumbled for one hour at 8RPM. This process results in large polydisperse multilamellar vesicles, to obtain SUVs, extrusion was performed. The large polydisperse multilamellar vesicles were extruded 21x through a membrane with 0.05 μm pore size, supported by two drain discs (Whatman Nucleopore Track-Etch Membrane, 19mm diameter, 0.05 μm pore size, with 10 mm Whatman PE Drain Disc).

2.1.4 Hybridisation of Deoxyribonucleic Acid (DNA)

The strands of DNA used with their label are shown in table 2.1, for simplicity we refer to the DNA used by their labels. The inert DNA is prepared by adding 10μL of 15 and 10μL of 16 to 90μL of HEPES buffer-2. Two complementary linker DNA strands are prepared as follows: For type A, 4μL of 17 and 19 are added to 90μL of HEPES buffer-2. For type B, 4μL of 18 and 19 are added to 90μL of HEPES buffer-2. Both the inert and linker DNA are placed in an oven at 94°C for 30 minutes and then cooled over night to room temperature in the oven, such that it cools slowly.

Label	Name	Molarity	Sequence
15	LongInert1	50μM	Double Stearyl - HEG(18) Spacer - 5'TT-TATCGC-TAC-CCT-TCG-CAC-AGT-CAA-TCT-AGA-GAG-CCC-TGC-CTT-ACG-A-3'
16	LongInert2	50μM	5'-TCG-TAA-GGC-AGG-GCT-CTC-TAG-ATT-GAC-TGT-GCG-AAG-GGT-AGC-GAT-TTT-3'
17	LongLinker A	20μM	Double Stearyl - HEG(18) Spacer - 5' - TT-TAT-CGC-TAC-CCT-TCG-CAC-AGT-CAC-CTT-CGC-ACA-GTC-ACA-TTC-AGA-GAG-CCC-TGT-CTA-GAG-ACG-CCT-GCC-TTA-CGA-*GTA-GAA-GTA-GG-3'-6-FAM*
18	LongLinker B	20μM	Double Stearyl - HEG(18) Spacer - 5' - TT-TAT-CGC-TAC-CCT-TCG-CAC-AGT-CAC-CTT-CGC-ACA-GTC-ACA-TTC-AGA-GAG-CCC-TGT-CTA-GAG-ACG-CCT-GCC-TTA-CGA-*CCT-ACT-TCT-AC-3'-Cy3*
19	LongLinker Backbone	20μM	TCG-TAA-GGC-AGG-GCT-CTC-TAG-ACA-GGG-CTC-TCT-GAA-TGT-GAC-TGT-GCG-AAG-GTG-ACT-GTG-CGA-AGG-GTA-GCG-ATT-TT

Table 2.1: *DNA strands used in the experiments. All DNA are manufactured by Eurogentech*

2.1.5 Functionalisation of the particles

23 μL of the SUVs are added to 77 μL of buffer type 1 and 100 μL of the sphere/cube suspensions at 0.05 w/v %. Often it was chosen that TopFluor-Cholesterol was added to the spheres and the DOPE-Rhodamine was added to the cubes. This solution is then tumbled for 1 hour at 8rpm. After this, it is again washed 1x to remove any excess SUVs. The solutions are added in excess, meaning the potential to cover a certain surface area is much greater than the surface area of the amount of particles present, this was roughly 17x the surface area.

In the final step, the prepared DNA strands are added to the lipid coated particles. To achieve a concentration of 1200 strands $/\mu m^2$, 40 μL of A/B are added, with 7.5 μL of inert DNA. Once the DNA has been added, the solution is then tumbled for 1 hour and washed with HEPES buffer-1.

2.1.6 Poly Acrylamide (PAA) Coated slides

To ensure the CSLBs are able to diffuse on a glass slide, poly acrylamide (PAA) coated slides are used. The protocol for preparing the slides is described in the following section. The coverslips (25mm diameter) are first sonicated for 10 minutes each in: MilliQ, ethanol, acetone, ethanol and MilliQ. Glass slides are stirred in 3M KOH for 30 minutes, rinsed 3x in MilliQ and then sonicated for a further 5 minutes in MilliQ and rinsed 2$\times$ in ethanol. The coverslips are ready to be coated in TPM. Ethanol is prepared with 1% v/v acetic acid and 0.5% v/v TPM, with the glass slides being immersed in this solution for 1 hour. The slides are again rinsed 3x with ethanol and placed in an oven for more than 1 hour at 80°. A 2 w/v% solution of acrylamide in water with 0.008 w/v% bis-acrylamide is then prepared, which is placed inside a glass chamber under vacuum for 30 minutes to remove most of the dissolved oxygen. The glass slides are then placed into the solution containing the acrylamide/bis-acrylamide. 0.035% v/v TEMED and 0.070% w/v APS are then added. This is stirred together under nitrogen for 1-2 hours for polymerisation. After this step, the glass slides are fully coated and can be stored in a fridge at 4°C. Before use with a sample, the glass slides must be washed in excess in ethanol and distilled water.

2.2 Observing the sample

To observe the sample, 7.5μL of functionalised spheres and 40μL functionalised cubes were pipetted into a sample holder containing 400μL of HEPES buffer-2 on a PAA coated slide. At these concentrations, this gave an even number of particles across the screen whilst imaging. Samples are imaged with an inverted Nikon Eclipse Ti-E confocal microscope with Nikon A1R scanhead (with galvano and resonant scanning mirrors). The objectives used to image were either a 60X water immersion (1.2 NA) or 100X oil immersion (1.4 NA) objective. The lasers used to excite the TopFluor and Rhodamine fluorescent dyes were 488 and 561nm, respectively which are passed through a quarter wave plate. Frame rates used were typically in the range of 20-25fps. Here, the confocal mode was mainly used to idenfity if particles had a homogeneous lipid bilayer, whilst brightfield mode was used to get the structure in focus and to videos.

To build the intended ring structures, Optical Tweezers (OT) are used, the advantage of this method is that the CSLB structures can be assembled manually. The OT used here is a homemade setup with a trapping laser manufactured by Laser QUANTUM (1064nm wavelength). Once a particle is trapped, it can be brought into contact with another particle such that they are given the opportunity to bind, often needing between 10-30 seconds for them to do so. Normally a sphere was chosen to attach to a particular location on a cubes face, since this was an easier operation to undertake. The time required to bind often depended on the concentration of DNA used, with higher concentrations of DNA resulting in quicker binding times. Upon successful binding of two initial particles, the next particles are added in a sequential manner from either side of the structure.

2.3 Tracking the particles in a ring structure

Image analysis software is widely employed in the field of bio & soft-matter physics to obtain information about the system at hand, for example particle or cell tracking. Whilst single particles with simple intensity profiles are normally fairly easy to image, the samples imaged in this project are both more complicated and have complex interference patterns due to the close proximity of the particles, which make the particles hard to track. Tracking joined particles is also a computationally expensive task since many iterations are spent refining the edges of the particles. Furthermore, the cubic particles used are asymmetric, which are slightly harder to track since many particle tracking software a symmetric intensity pro-

file. The problem here is therefore twofold; structures with both complex interference patterns and asymmetric particles. In the following two subsections, methods to try to track the system are presented.

2.3.1 DeepTrack

One attempt to solve this was to use new recently developed tools, the first being a software package in python called DeepTrack [14]. DeepTrack uses Neural Networks (NN) to learn and calculate positions of particles. A NN is a subdivision of machine learning algorithms that are adapt at classification problems and more recently have been adapted to digital microscopy [15]. In a simple way, a NN is a series of (multi) layered nodes connected by weights. The purpose of a NN is to train these weights, such that when an input is received, a correct output is given. An example is giving an image as an input, and a yes or no answer as an output: is this a picture of a dog? During training, weights are penalised for guessing the wrong answer, so the goal of the NN is to minimize this, which can be quantified in a loss function. To learn a problem efficiently, both suitable and a sufficiently large amount of training data must be used. Here, the data must be relevant to the problem at hand as well as there being enough data to learn from, normally thousands of images are used in training a NN. The data must also be relevant, since training on a ”bad” dataset can lead to a network that cannot identify an input correctly.

To create both the training and test data set to learn from, DeepTrack uses a combination of scatterers and optics to define an image, which the user can adapt to their own settings. The aim of this is to create an image that is as close to the experimental data as one can get. A generator is used to create new instances of this image, with random positions and orientations, which ensures every data point in the dataset is different. Generated examples are shown in Fig. 2.2 (b,c,e). The NN is learning to associate the position, X-Y coordinates with surrounding pixel values. The training data set is used here since it contains both the image and the particles coordinates, so the NN can learn these patterns. In terms of minimizing the loss function, large distances between the guessed centre and the real centre of the images are penalised. These tests are validated on a validation set (a subset of the training set) to see how well the NN currently performs. These learning steps are iterated over many times until the validation accuracy, how accurate a guess on the validation set is, is sufficiently high, roughly 90% accurate. Once this step is completed, the NN can be tried on the experimental data, with the aim that if the

experimental data "looks" close to the training data, DeepTrack should be able to correctly predict the position of the particles.

A Convolutional Neural Network (CNN) was used to track spheres to familiarize with the software. To get a more representative picture of the experimental data used here, a cubic shaped scatterer had to be implemented into the source code, since DeepTrack only includes sphere or ellipse scatterers. A cube can be approximated by taking the equation of a circle and raising to higher powers $x^m + y^m = 1$ [16]. Sphere and cube scatterers are shown in Fig. 2.2 (c,e) with an overlay of the real centers and tracked centers. During training the accuracy of tracking spheres reached around 98% and on unseen generated images a difference of $\sim$ 0.5 pixels between the real center and the tracked center. Fig. 2.2 (a) shows the accuracy and validation accuracy over 50 epochs (itterative time step in a NN) when learning to track a sphere. When tracking on experimental images, results often varied, sometimes tracking close to the centre, other times tracking outside of the sphere, Fig. 2.2 (d) shows the sphere being tracked on the edge of the particle. For training on the cubes, the validation accuracy reached around 97%, with a difference of $\sim$ 0.6 (Fig.2.2 e) pixels between the real center and the tracked center. When tested on an experimental image, Fig. 2.2 (f), tracking was often near the center of the particle.

The next step was to track multiple particles at once, rather than track single particles. To do this, a U-Net is used instead of a CNN, since a CNN can only return a set number of outputs, rather than an array of outputs (e.g 2D array of multiple particle positions). The training data set then had to be set up to represent the experimental data, that is to arrange each particle into a ring. This could be done, however problems were encountered when updating the position and orientation of the individual particles, which were both not updating correctly. Furthermore, attempts to change the optical settings, which affect how bright or dark an image is, were also not updating correctly. Performance of a NN is closely linked to how well the synthetic data represents the experimental data. One way to check this is to create a histogram of pixel values (0-255 for a gray scale image) and see where the peak values lie. This is important, since the NN will learn to associate a position, with surrounding pixel values, i.e is the centre of the particle a bright spot with a dark ring around it. If these pixel values do not match well, then the NN is likely not to track particles correct, since it has learnt badly. Histograms of the synthetic and experimental data for a sphere, and a 3×3 structure are shown in the appendix. For an image of a single sphere, settings affecting the brightness of the image could be changed easily and histogram peaks could be made to overlap. However,

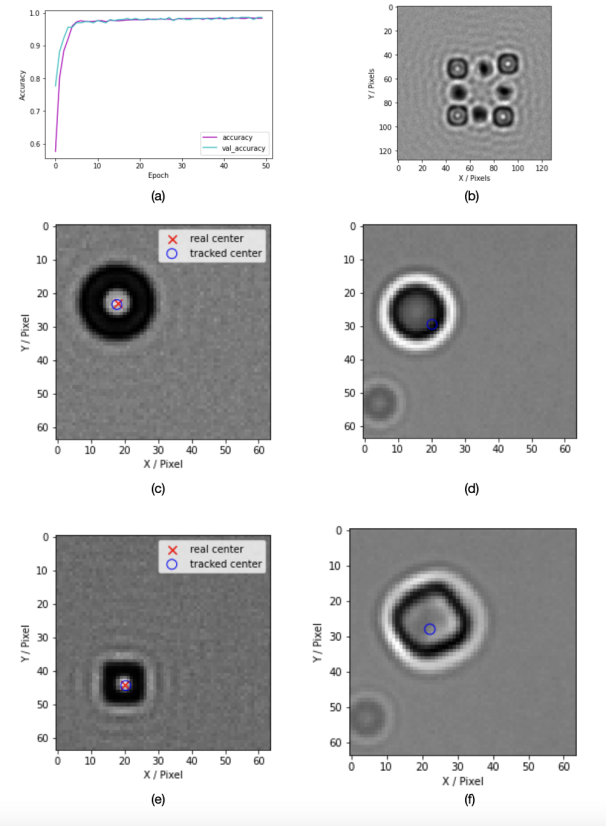

Figure 2.2: *(a) The training accuracy and validation over 50 epochs for tracking on generated images of spheres. (b) a generated 3 by 3 structure used in the DeepTrack training. (c,e) shows the real and tracked center on unseen, but generated data for a sphere and cube shape. (d,f) tracking on experimental data of a sphere and cube respectively.*

for the 3×3 structure, settings were not changing, meaning that the peaks for the histograms were at different pixel values. Because the software was not updating correct, this meant that the histogram of the synthetic data set was also not able to change, in the time spent working with this, no fix was found.

When tracking multiple particles, results were often very poor, either not tracking the particles at all, or just tracking the edge of the particle rather than the centre. Fig. 2.3(b) shows DeepTrack returning tracked positions of the background and cube edges rather than the cube itself. There is another reason why DeepTrack also failed at this point; for use in a U-Net, a binary representation of the image is used, done by creating a mask of the image. Here, because of the complexity of the intensity

profile of the experimental image, incorrect outlines of the particles are made, shown in Fig. 2.3 (c). This meant that when calculating the centre position from the outline, incorrect positions are given. This is a problem inherent to creating a mask from the brightfield image, it is possible that by using a confocal image instead, clearer outlines of these particles could be given. Due to the lack of time remaining in the project and with the current problems present, other tracking methods were tried instead.

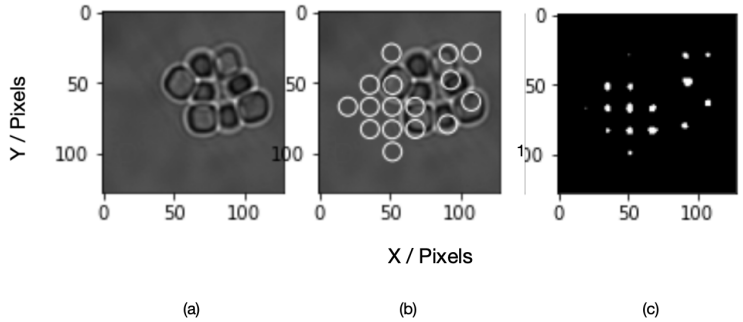

Figure 2.3: *(a) Experimental data to be tracked. (b) Tracking of the particles performed by DeepTrack. (c) The mask generated by DeepTrack of the image*

2.3.2 Other particle tracking methods

As for the next attempt at automated tracking, TrackPy [17] and ClusterTracking [18] were tried and tested. TrackPy is another widely used tracking algorithm, a python adaption of the Crocker-Grier algorithm [19]. Briefly, this works by assuming the particles position is given by a brightest pixel and searching for this pixel. Once found, it compares this pixel to other neighboring pixels where methods to estimate a refined location are then applied. Whilst TrackPy works well for spherically symmetric particles and more often, confocal images (see [9]), attempts to use TrackPy for this project also did not work.

The problem here was that TrackPy was tracking the bright spots inbetween particles rather than the particle itself, with an example shown in Fig. 2.4. Whilst the fact that the centre spot is the particles brightest spot is a reasonable assumption for some colloidal experiments, this may not be suitable for tracking cubic colloids. Other algorithms could be more suited to tracking these cubic colloids [20] (supplementary information). As can be seen in some images (Fig. 3.1) the brightest part of the particle is not the centre, but rather the outline. This could be inverted by setting the function: ”invert = True” on, where TrackPy instead tracks the darkest

points, however this still did not work. The problem with applying this algorithm to a ring of sphere and cubic colloids is twofold. First, the intensity profiles of the cubic particles are not uniform, the edge of the particle is brighter than the centre, with another dark outer edge coming from the light intefering with the particle. Furthermore, the brightest/darkest pixels within the centre region of the particle are not necessarily the centre position. It was also found that the intensity of profile of both the spheres and cubes change with the focus of the microscope. This causes a problem, since it means that this also changes where the brightest/darkest spots of the particles are, adding to the complication of associating the brightest/darkest spot with the particles centre. Furthermore, when two or more particles are bound, there are often interference patterns as a result of the light diffracting off of/transmitting though the particles. This results in much more complex intensity profiles surrounding the particles, which are in turn harder to track correctly. Moreover, particles that move out of the plane of focus also have a completely different intensity profile compared to a particle in focus. These particles appear "see through" rather than having a harder boundary and therefore do not have the apparent bright and dark spots.

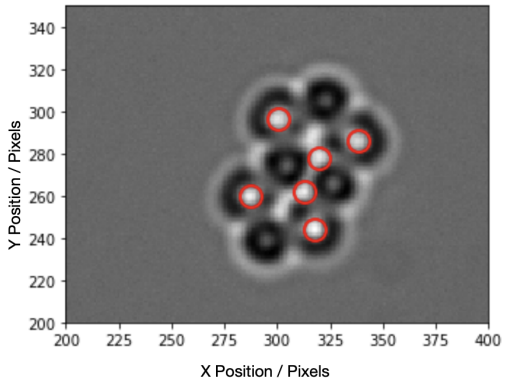

Figure 2.4: *TrackPy was often tracking both spheres and the bright spots between the particle as shown here. This is because TrackPy searches for the brightest pixels within a given vicinity. Because of the diffraction of light off of the particles, bright spots often appear between particles. This image is taken slightly out of focus to create a smoother intensity profile.*

One attempt to work around this problem was to instead take videos of the sample that were slightly out of focus. This created a smoother intensity profile, since it removed some of the artifacts that stem from the more complex light interference. Details of the edges are lost here, but since the

Version of December 16, 2021– Created December 16, 2021 - 22:24

algorithm tracks the brightest spots, this in turn aids this identification. Using out of focus images instead, TrackPy was able to recognise some of the spherical colloids, however not the cubic colloids for a given image (vice-versa was possible when setting invert = ”false”). Whilst this was a step forward, this was not a full implementation of automatic tracking that was sought after, where tracking all particles accurately is required for the analysis. There were also software issues present, one being that identical codes ran on different PCs were returning different results, one PC tracking and other receiving an error.

ClusterTracking is an adaptation of TrackPy, with specific implementations to track overlapping features of images, relevant here because colloids are in close contact with one another. However, using this software was returning similar results; namely is was tracking the bright spots that were in-between particles rather than the particles themselves.

As another attempt on automated tracking, the software package Canny edge was used. Canny edge detection is a multi-step algorithm that detects edges within an image. The first steps in the algorithm are reducing the noise in the image and then calculating an intensity gradient, which is how much does each pixel changes value compared to its neighbors. Using this, each pixel is then compared to its neighbours to check if it is a local maximum, where threshold is then applied to create an edge for the image. The result is a binary image, with a pixel either constituting an edge or not an edge. By using this edge, tools from SKlearn are used to calculate the centre from this edge. Due to the complexity of the intensity profiles, it appeared that canny edge had trouble figuring out what was the edge of the particle even with different thresholds used, shown in Fig. 2.5. This is similar as to why DeepTrack was failing to track particles, Fig. 2.3, both of these methods rely on a clear outline of the particle, whereas due to the complex light patterns present, outlines are hard to define.

Because of these issues presented, a better method could have been to use confocal images in the tracking software, rather than using images captured in brightfield mode. Here, clearer edges of the particles can be identified, since the fluorescence is only coming from the edge of the particles, rather than the whole sample being illuminated. These are easier to track using software such as TrackPy

After exhausting the options stated above, it was instead decided to use manual tracking using ImageJ. Tracking using ImageJ can be done simply by using the following steps; first select the outline of each particle (using the circle or polygon selector), then calculate the centre of the particle (X,Y) using an inbuilt function. Because this is a manual process, it is rather slow, meaning that fewer frames of each video were captured. As many

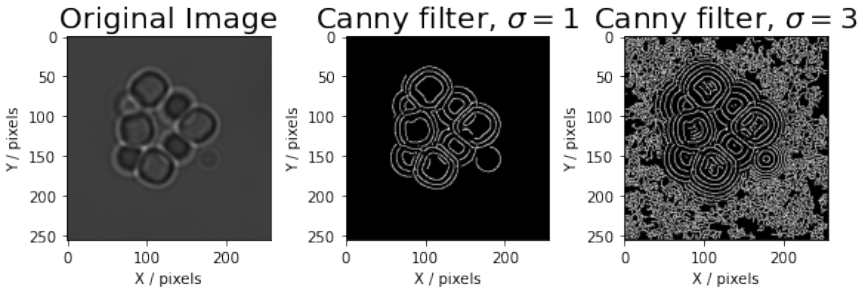

Figure 2.5: *Canny edge outlines with different filter values. With increasing σ values, more and more details are picked up and used as edges. Even with a low σ = 1 value, edges are not very representative of the real edges of the particles and are often lost when particles are in contact with one another.*

frames were analysed as possible, however the total number of frames analysed is in the low hundreds rather than the many thousands.

Chapter 3

Results

In this chapter, we first present the structures made via the protocol stated in the methods. We show flexibility in the structure via angle analysis, where experimental data is compared to a model system. Finally, we show that the structural changes can be visualised by mode analysis.

3.1 Structure Design

By using the optical tweezers, CSLBs can be brought close together in a precise manner such that they have the chance to bond together. By placing the CSLBs in a sequential manner, cube-sphere-cube, with the next sphere attached being at a right angle to the previous, structures such as the one shown in Fig. 3.1 can be made. This results in a ring-like formation with an open space in the middle. Not only were the resulting structures flexible, displayed by the ability of the structure to take different conformations, but the spheres were also restricted to a single face of each cube. In the next section, we show the flexibility of the cube-sphere-cube and sphere-cube-sphere joints by angle analysis, and how in some cases this is limited by stuck joints. The structural changes are also then explored by using mode analysis.

3.2 Structural Analysis

3.2.1 Model System

In this analysis we propose to look at what angles are produced by the system, allowing some deductions as to what are the most likely conforma-

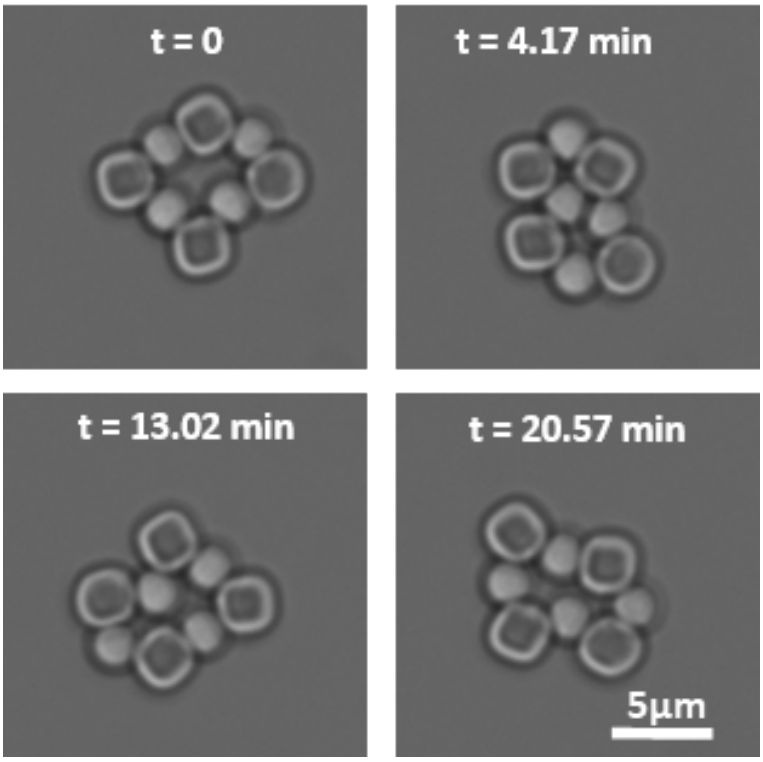

Figure 3.1: *Assembled 3x3 open-square structure from sphere and cubes. This is an example of how the conformations of the structure can change over time*

tions and what are the conformational constraints. The structure considered here is shown in Fig. 3.2, the side angles are highlighted as a, c, e, g. These are the angles made by the cube-sphere-cube colloidal joint. The corner angles are highlighted as b, d, g, h and represent the sphere-cube-sphere colloidal joint. Here, it is assumed that all "like" angles behave in the same way, $a = c = e = g$ and $b = d = g = h$. This assumption can be made since there is rotational symmetry in the system, however it should also be considered that this also depends on the quality of flexibility of the joint. This is dependent on the mobility of the lipid bilayer, if the lipid bilayer is damaged or immobile, then a joint can get stuck, meaning one joint can behave different to the others. Variation is expected since this quantitative analysis only relies on geometry and real samples have some differences to the model system such as curved edges and rough surfaces, both of which affect the flexibility and constraints. All angles are calculated relative to the centre of each cube/sphere particle.

To start, we first consider the angle created by a sphere on the face of a cube, since it is this angle that forms the basis of the corner/side angles.

The maximum and minimum angles of the corner and side angles can easily be calculated by simple geometry. A schematic of the whole model structure, as well as the corner/side angles are shown in Fig. 3.2. By using the relation $\tan(\phi) = X/L$, where $L = r + d$, with r being the radius of the sphere and d is half the length of the side of a cube, with $r = d = 1\mu$m. In bonding between a sphere and a cube there is a patch size caused by many linker DNA binding together. For ease of analysis below, we assume that the patch size is simply the contact point between the sphere and the cube. In reality, the patch does have a finite size, but is also something that affects the membrane, thus affects the extent to which the patch touches the edge.

The maximum angle between the centres of the cube & sphere and the edge of the cube face is $\phi = tan^{-1}(1/2) = 26.6^\circ$, 3.2 (top right). This value is then used to calculate what are the minimum and maximum values of the side and corner angles.

The side angle can be considered by looking at the initial building block 3.2 (top right), with the angle originating from the sphere. This is half of the angle that would be originating from the whole side angle, therefore can be written as $\theta^{side} = \theta/2 = 90 - \phi$. Since $90 - \phi = 90 - 26.6^\circ$, $\theta^{side}_{min}/2 = 63.4^\circ$ and so $\theta^{side}_{min} = 126.8^\circ$. The angle θ^{side}_{max} can be calculated by $360 - 2 \cdot 63.4 = 233.2^\circ$.

The maximum and minimum corner angles are calculated as follows $\theta^{corner}_{max} = 90 + 2 \times \phi$, and $\theta^{corner}_{min} = 90 - 16.6 = 73.4^\circ$ (for derivation see appendix). θ^{corner}_{min} is smaller here since two spheres can touch if they approach the same apex.

Since the cube-sphere joint acts as a planar slider (see Fig. 2 m,n in [9]), the first quantity to look at is the position of the centre of the sphere (attached to a cubes face) relative to the centre of the cubes side and to generate a probability, $P(X)$, that a sphere is at a given position on the cubes surface. $P(X)$ can be calculated by choosing a given cube and sphere and determining the positions of their centres, as well as the rotation of the cube. Using the rotation of the cube relative to the x-axis, the two particles are then rotated by the angle at which the cube is at, about the centre of the cube. To generate $P(X)$, a normalised histogram of the difference in heights of the centers of the sphere/cube $X = X^{sphere} - X^{cube}$ is made, shown in Fig. 3.3. This figure shows the motion is indeed restricted on the face of the cube and is within the expected bounds (± 1). However, due to the lack of data, it does not clearly show the most preferred position of the sphere on the face of the cube. The most reasonable assumption to be made from the planar description is to use a uniform distribution $P(X)$, with

Version of December 16, 2021– Created December 16, 2021 - 22:24

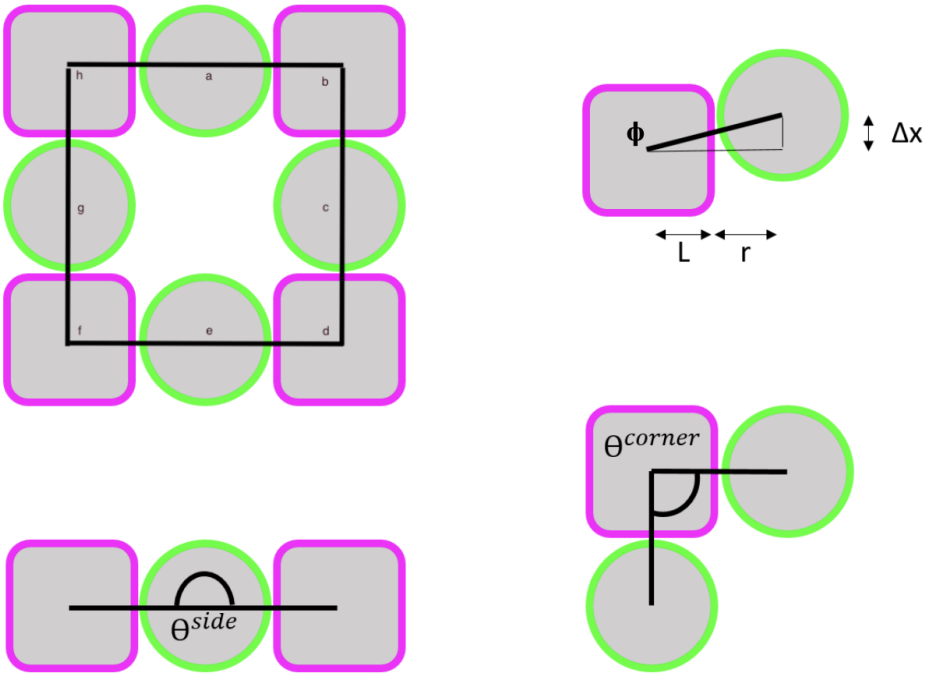

Figure 3.2: *(top left) Schematic diagram of the 3 by 3 structure constructed out of spherical and cubic colloids. (top right) each angle can be de-constructred to a simple building block that is considered here. (bottom left) A cube-sphere-cube joint constructs the side angles, where as (bottom right) a sphere-cube-sphere joint constructs a corner angle*

$$P(X) = \begin{cases} q = 1/2 & : x \in \{x_{min}, x_{max}\} \\ 0 & : \text{otherwise} \end{cases} \tag{3.1}$$

Where $q = 1/2$ comes from integrating $P(X)$ from $x_{max} = 1$ to $x_{max} = -1$ and assuming all values in between are equal to 1, they are equally likely. The reported errors on the position are $\pm 0.02\mu m, 0.04\mu m$ for the x, y of a sphere respectively and $\pm 0.03\mu m, 0.02\mu m$ for the x, y of a cube respectively. These were calculated from the standard deviation from repeat measurements of the position.

Using this assumption, the next step is to consider what are the angles made by the structure. By using $P(X)$, a transformation of variables can be made to obtain a distribution of the angles made by the structure, $P(\theta)$. $P(\theta)$ represents the probability that the side/ corner joint has an angle θ with respect to the centre of their positions. Here, we make the further assumption that cubes are fixed in space and do not rotate

Version of December 16, 2021– Created December 16, 2021 - 22:24

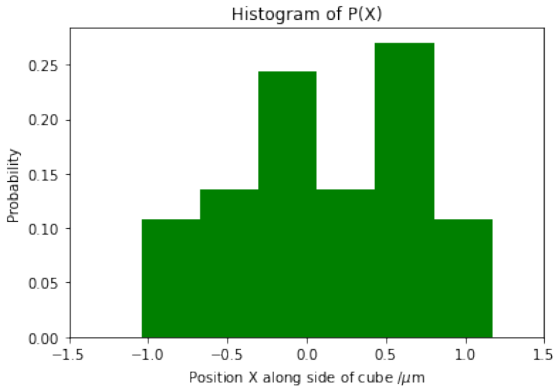

Figure 3.3: *Distribution of the position of a sphere on the face of a cube, with X being the difference in heights of the centers of the particles.*

with respect to one another. This gives an idea to the preference of the state that the structure lies in. The transformation can be calculated as follows: $P(\theta)d\theta = P(X)dX$, where the new distribution is calculated as $P(\theta) = f_\theta(\theta) = f_X(v(\theta)) \cdot |v'(\theta)|$, with $v(\theta)$ being function in terms of theta. Using

$$v_{corner}(\theta) = \tan^{-1}(\theta) - \frac{\pi}{2} \tag{3.2}$$

and

$$v_{side}(\theta) = 2\tan^{-1}(\theta - \frac{\theta}{2}) \tag{3.3}$$

The resulting distribution for the corner and side angles are:

$$f_\theta(\theta) = p(\theta^{corner}) = \frac{2q}{(\theta - \pi/2)^2 + 1} \tag{3.4}$$

and

$$f_\theta(\theta) = p(\theta^{side}) = \frac{q}{2(\theta - \pi)^2 + 1} \tag{3.5}$$

These distributions represent the most likely angles that are made by the structure and therefore the conformations that are expected of the structure. By plotting these functions (Fig. 3.4), we therefore expect that the most probable structure is an open square, due to the angles 180° for the side and 90° for the corner being most likely. This comes from the fact that whilst for sphere on the face of a cube, there is a uniform distribution, the angles calculated from this are not uniformly distributed, but peaked towards the centre of each distribution. These represent the most probable angles for the structure to hold, and therefore help define what are its most probably conformations.

3.2.2 Angle Analysis

Fig. 3.4 shows the probability distribution of corner and side angles for 3 samples (each angle is plotted individually), compared to the PDF of the model system defined by eq. 3.5, 3.4. Most of the data does show some kind of peaked distribution, however due to the lack of data, it is hard to make a concrete inference from this. There are two immediate observations, the first is some narrow single peaks, caused by stuck angles, which will be discussed in more detail below. The second is a difference in the approximate width of the distributions, if we compare nd001 and nd069, it can be seen that the distributions in nd069 are much narrower than that of nd001. This shows a difference in the flexibility of the two structures, with nd069 being less flexible since there is less variation in the angles given.

Fig 3.5 is a histogram of the total data analysed. Even though looking at individual angles can help identify stuck angles, looking at the total data can give indications of the overall structural preferences of the samples. Most of the data lies within the bounds of the expected shape, as well as the peaks of the angles being close to the centre. This could also be a consequence of a biased sample where data file nd001 had 120 frames analysed, where as nd002 and nd069 had 51 and 41 frames analysed, respectively. These results do show that in general, because of the restricted movements of the spheres on the face of the cube, there are restrictions in the maximum and minimum angles that are made by the structure, with angles towards these maximums being less likely.

Whilst most of the data follows a peaked distribution and lie within the expected bounds, there are some obvious exceptions to this. There are many angles which are not centered around the expected angles (90° for corner and 180° for side angles), as well as angles with very narrow distributions. One of the reasons for this is that the joint could be stuck, meaning this joint is not flexible and thus cannot move. The stuck angle acts as a defect in the structure, restricting the movement of the adjacent particles, in turn increasing the rigidity rather than making it flexible. Joint flexibility can be calculated from the mean square angular displacement [9], however, diffusion for cubic colloids need to be defined properly before being used. Furthermore, more data would be needed to make a conclusion whether the presence of a stuck join influences the flexibility the other joints in the structure, A stuck angle is generally cause by an immobile part of the lipid bilayer, meaning the DNA on the surface cannot diffuse and thus a joint is not flexible. The distribution of this angle is also characterised by a very narrow width, compared to flexible angles whose

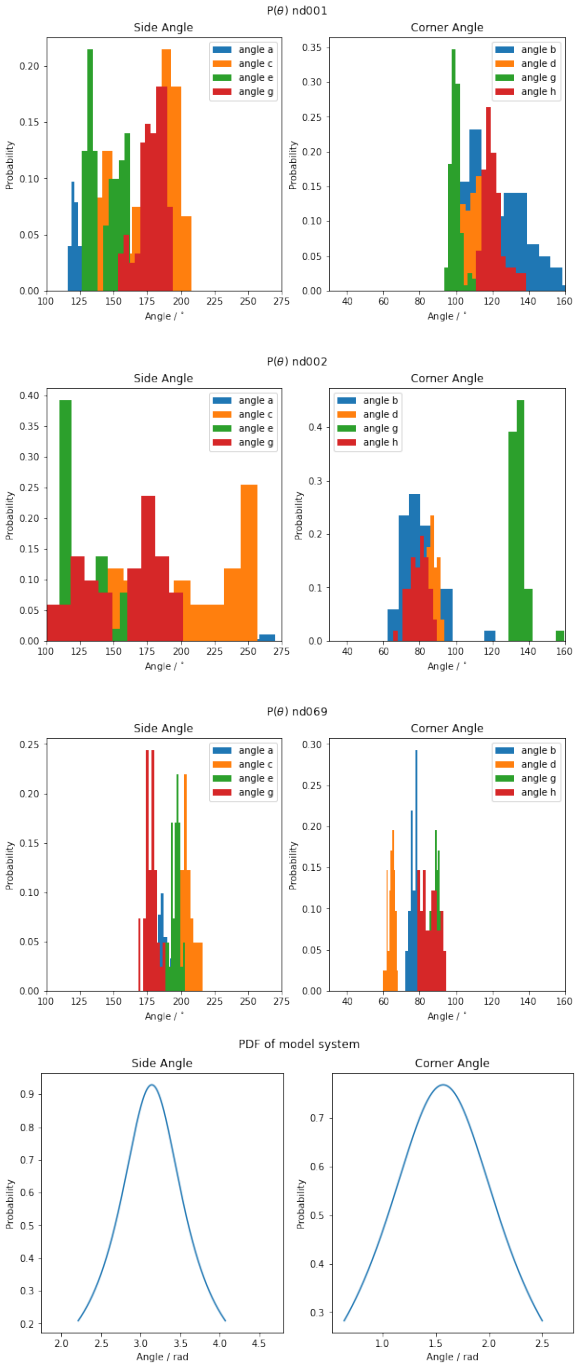

Figure 3.4: *Probabilities of an angle θ occurring in the structure for corner and side angles. The bottom plot shows the probability density function of the model system.*

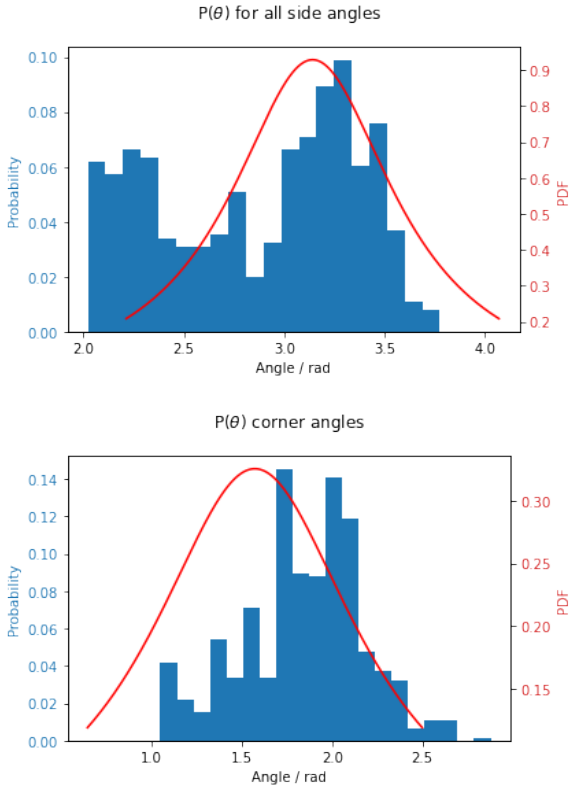

Figure 3.5: *Probabilities for both side and corner angles occurring with the model probability density function. Data here is an accumulation of the data shown in Fig. 3.4, which instead gives an oversight as to how the structure behaves over multiple samples, rather than individual angles in individual samples.*

distribution widths are much larger (e.g angle g in nd002). There are many reasons for a joint becoming stuck; one of the causes is a broken and/or non-uniform lipid bilayer. Normally, these were identified beforehand using the confocal microscope such that only particles with a uniform bilayer are chosen to be building blocks for the structure. To confirm if this is the case, fluorescence recovery after photobleaching (FRAP) experiments can be done to investigate the mobility of the lipid bilayer [12]. An experiment like this is difficult to do on individual particles on coated slide since they diffuse very quickly, so a sample prepared on a glass slide should be used instead such that it cannot diffuse. Another reason behind an immobile bilayer could due to the surface of the particle itself, where rough surfaces hider the mobility of the bilayer [9].

Often, flexible structures were hard to come by for multiple reasons. For one, even though a sample looked good on confocal mode, particles

were sometimes getting stuck upon binding. This could happen for the first two particles to attach, or possibly even the last particle to attach. This meant that sometimes building was a slower process than originally thought, since it was sometimes hard to obtain a fully flexible structure.

It is known that the joint flexibility is linked to the DNA concentration [9], however, it could also be that the age of the DNA stock also has an effect of the flexibility. This was found when changing DNA stock from old to new and finding that much lower concentrations of DNA (i.e 400 strands/μm^2) were needed to make flexible structures. The reason for this could be the slow denaturing of the DNA when constantly freezing/melting the DNA when taking stock from the freezer, however more data would be needed to confirm this.

3.3 Mode analysis

The vibrational modes of a structure can be extracted from fluctuations of a structure by means of mode analysis [21]. The vibrational modes here refer to larger structural changes (such as a shear mode), which are a response to thermal fluctuations. The vibrational modes of a structure (a lattice for example) can be extracted by computing the eigenmodes of the covariance matrix of the particle positions. By plotting the eigenvectors of the covariance matrix on the average positions of the particles, these modes can be visualised since they show the average direction for each particle in a given mode. This section runs through how the mode analysis is conducted, proofs of the following can be found in the appendix of [21].

Starting with a system of N particles with trajectories $|r(t)\rangle$ and a statistical reference $|r_0\rangle = \langle |r(t)\rangle \rangle$ over a time τ, with $\langle . \rangle$ referring to an average over time. A displacement vector can be defined as $|\delta r(t)\rangle = |r(t)\rangle - |r_0\rangle$, where in the average translation and rotation of the structure are taken out. These are removed since these cost no energy (in comparison to a shear mode, which does cost energy) and so the modes can get mixed up with the other modes of the system. The covariance matrix of these displacements is the average (over time) of the inner product of the displacements:

$$C_p = \langle |\delta r(t)\rangle \langle \delta r(t)| \rangle \tag{3.6}$$

wherein the long time limit:

$$C_p |\lambda_q\rangle = \alpha_q^2 |\lambda_q\rangle \tag{3.7}$$

C_p is a real and diagonalisable matrix, where α_q is the amplitude of the projection of the initial condition on the mode $|\lambda_q\rangle$. The diagonalisation of the matrix C_p provides the vibrational modes of the system. By plotting each eigenvector with corresponding eigenvalue, one can find the vibrational modes of the system. It was noted that for the application to the systems presented here, enough frames must be analysed (roughly 100 as the minimum), where each frame must be statistically independent from the previous, showing no correlation in the system [21].

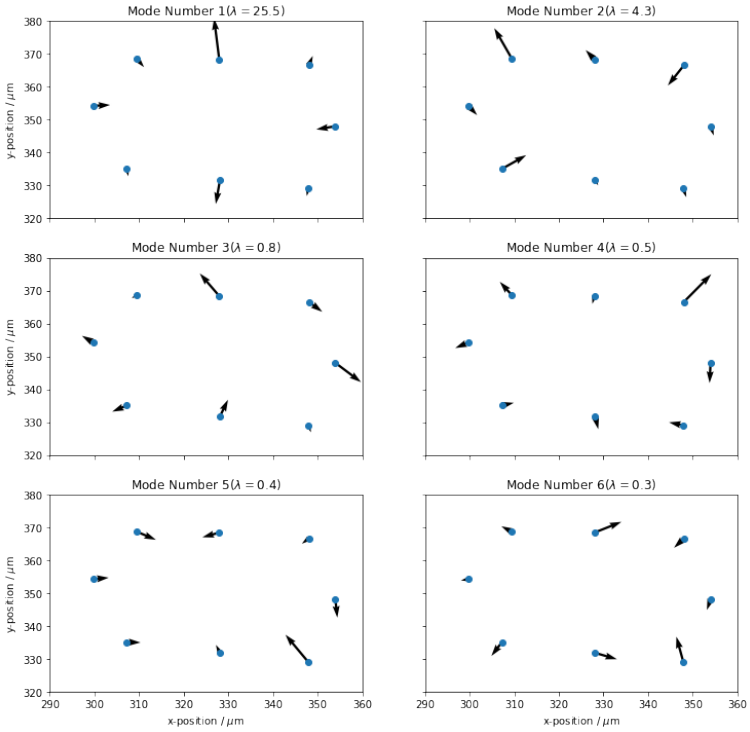

Figure 3.6: *The first 6 modes taken from a video of the structure. Each mode shows the average position of the particles, with the eigenvectors plotted with their respective eigenvalue (λ). For a given mode, there is a preferred direction for each particle, which is given by the eigenvector. By plotting each eigenvector for each particle, the overall movement of the structure can be seen. Data is obtained from the nd001 file with 121 frames analysed.*

The first 6 modes are shown in fig. 3.6, there are in fact 16 modes possible, coming from the 8 particles having 2 position components (x,y). As mentioned earlier, plotting the eigenmodes reveals the average correlated motions of each particle for a given mode, here in reference to the average particle position. The data was adapted by taking out overall structural translations and rotations. Translations are taken out by calculating an

average position over all times for each particle, and subtracting the displacements from a reference frame (frame 0). Rotations are taken out by calculating an average angle of the line connecting the particle center with the structures centre of mass and the x-axis. The structure is then rotated by the average angles between two frames.

Rotations and translations are taken out from the displacements since their response to thermal fluctuations is not harmonic, they therefore show up in the mode analysis with non-zero energy (the ideal case is that they are zero energy). If these modes are not taken out, they then mix with other low energy modes. Low energy modes, such as a shear mode, may not be entirely harmonic in response, but show up well in the mode calculations.

With the assumption that at equilibrium, each mode has a frequency ω_q and amplitude α_q, each mode has the same energy, $1/2k_BT$. The eigenvalues λ_q of the matrix C_p can be related to the frequencies $\omega_q^2 = k_BT/m\lambda_q$. A mode that has a low frequency has a high amplitude. The energy of each mode can then be given as:

$$E = \frac{1}{2}\alpha_q^2\omega_q^2 \tag{3.8}$$

The modes with the highest eigenvalues, modes 1 and 2, are here showing breathing modes, with opposite particles heading in opposite directions. These modes cost the least energy after translations and rotations, with the result being that they have the highest amplitude. However, in other cases (e.g mode 5) movement looks more random, both in direction and magnitude. One of the main reasons for the lack of visibility in the modes is the lack of data, stemming from a low number of frames and a short length of time the frames are taken over (5 minutes). It is possible that because the video taken was quite short, only some of the possible conformations were explored by the system, and thus more compression/shear modes are not present. Furthermore, due to the tracking precision and optical resolution, some fluctuations are too small to be seen. We should expect some more lower energy shear modes before seeing the higher energy modes that are more noisy.

The dynamical matrix D is closely related to the stiffness matrix K, $D = K/m$, with m being the mass of each particle. ω_q^2 are the eigenvalues of the matrix D, with κ_q being the eigenvalues of the stiffness matrix K. ω_q and κ_q can be related by $\omega_q^2 = \kappa_q/m$. A higher value of ω_q also corresponds to a stiffer mode. More time is needed to interpret the results in relation to the stiffness matrix, however this could be an interesting avenue to explore.

Chapter 4

Conclusion

In this thesis we demonstrated a strategy for constructing a ring-like flexible colloidal structure. Whilst successfully making the structures, there are still many problems present which can be improved upon. The angle analysis revealed that whilst the system behaves close to the model system, with the angles being mostly within the bounds and showing a peaked behaviour, it also shows the imperfection of the system. This is highlighted by stuck angles which are shown in the histogram by a distribution with a very narrow width. Stuck angles are often caused by immobile lipid bilayers, with one of the causes being a ruptured or broken bilayer. Fully flexible samples were often hard to make since the behaviour of the samples was changing frequently. Even under the same preparation two samples could behave differently. Moreover, stuck angles were a frequent occurrence when making these samples. We also show that shape changes of the structure can be shown via mode analysis, revealing compression and shear modes present in the structure.

One of the main improvements for this project would be to take the videos in confocal mode such that automatic particle tracking (by use of TrackPy for example) can be done. The reason why most data was taken in brightfield mode was because it was going to be used in DeepTrack, which ultimately did not turn out to work. This would have vastly improved the quality and the amount of data genererated from the sample. This could have made both the shape of the distributions and the direction of the modes more clear. There could be more checks as to wether the lipid bilayer is mobile over the whole sample, especially in the cube colloids, where the smoothness of the face can affect the bilayer mobility.

The model can be improved in a few ways to make it more representative of the real system. In the model system, the cubes are always parallel

to an axis, so rotations of the cube can be taken into account. The patch size could be taken into account more accurately, such as using its proper size and considering how much it can bend around a cubes corner (which is smooth rather than a sharp edge). This would affect the extent to which the sphere can move on the face of the cube, likely making the move-able distance smaller. Many of the above could be implemented if there was more time, which was unfortunately not possible during the time of this project because so much time was spent creating a good sample.

However, there are potentially other exciting avenues to explore with this project such as altering the linker length and particle sizes. Changing the linker length has been shown to affect the diffusion of the DNA linkers bound to a lipid bilayer, with the concequence that a spherical colloids could diffuse around the edge of a cube. The size of either the cube or the sphere can also be changed, this would affect distance the spheres can diffuse on the face of the cube, which could also affect the angles created by the structure. These could reveal new modes or be tuned as such to mimic other molecules. Larger structures, although potentially difficult to make are also a possibly interesting route to explore, where new deformations in the structure could take place. Hierachical structures could also be made, by using these 3×3 as building blocks for larger strucutres. These could both act as other model systems or for potentially other applications.

Appendix

Minimum Corner Angle

Assuming the spheres touch at 45° and using $tan(\alpha) = \frac{\delta x}{L+r}$, where α is the angle between the $x-$axis and the centre of the sphere and $L = r = 1$. Now: $cos(45) = \frac{r}{2l-\delta x}$, so $\delta x = 2l - \frac{r}{cos(45)}$. Inserting this into the expression for $tan(\alpha)$ gives $\alpha = tan^{-1}(\frac{2-\sqrt{2}}{2}) = 16.3°$.

Histograms of pixel values in DeepTrack

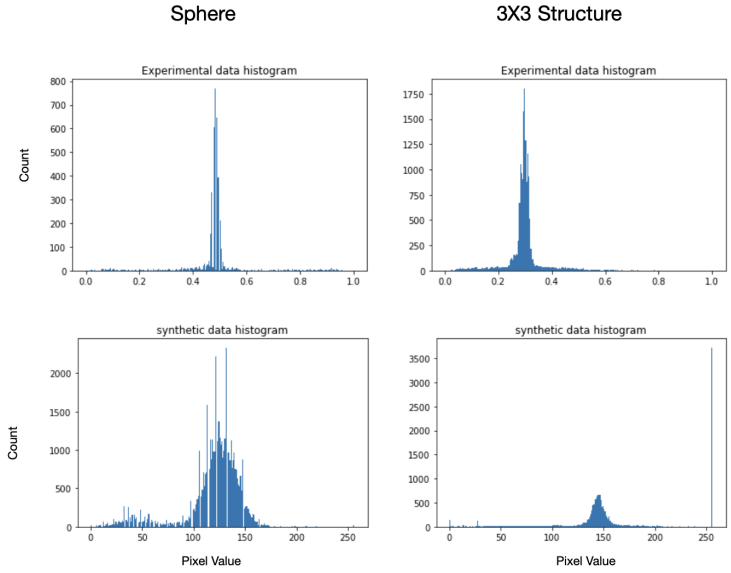

Figure A1: *(left) shows the histogram of experimental and synthetic data of a sphere. (right) Histogram of a 3×3 structure. There is a clear difference between the peaked values of the 3×3 structure, meaning that the U-Net was learning off of different pixel values to that which are present in the experimental data. When the peaks overlap, as it does for the sphere, then tracking is often much more accurate.*

Version of December 16, 2021– Created December 16, 2021 - 22:24

Bibliography

[1] J. Klier, J. Bohling, and M. Keefe. "Evolution of functional polymer colloids for coatings and other applications". In: *AIChe Journal* 62 (2016), pp. 2238–2247. DOI: 10.1002/aic.15211.

[2] F. Wei, T. Zhong, and Z. Zhan. "Self-assembled Micro-nanorobots: From Assembly Mechanisms to Applications". In: *ChemNanoMat* 7 (2021), pp. 238–252. DOI: 10.1002/cnma.202000608.

[3] D. Babic, C. Schmitt, and C. Bechinger. "Colloids as model systems for problems in statistical physics". In: *Chaos: An Interdisciplinary Journal of Nonlinear Science* 15 (2005), p. 026114. DOI: 10.1063/1.1839311.

[4] S. Swinkels, S. Stuij, and P. Schall. "Revealing pseudorotation and ring-opening reactions in colloidal organic molecules". In: *Nature Communications* 12 (2021). DOI: 10.1038/s41467-021-23144-6.

[5] P. Kowalewski et al. "Probing the Structure, Pseudorotation, and Radial Vibrations of Cyclopentane by Femtosecond Rotational Raman Coherence Spectroscopy". In: *The Journal of Physical Chemistry* 119 (2015), pp. 11215–11225. DOI: 10.1021/acs.jpca.5b07930.

[6] W. Li, H. Palis, and R. Merindol. "Colloidal molecules and patchy particles: complementary concepts, synthesis and self-assembly". In: *Chemical Society Reviews* 49 (2020), pp. 1955–1976. DOI: 10.1039/c9cs00804g.

[7] R. Verweij, D. Kraft, and P. Moerman. "Flexibility-induced effects in the Brownian motion of colloidal trimers". In: *Physical Review Research* 2 (2020). DOI: 10.1103/physrevresearch.2.033136.

[8] J. Yguerabide, H. Epstein, and L. Stryer. "egmental flexibility in an antibody molecule". In: *Journal of Molecular Biology* 51 (1970), pp. 573–590. DOI: 10.1016/0022-2836(70)90009-4..

[9] I. Chakraborty et al. "Colloidal joints with designed motion range and tunable joint flexibility". In: *Nanoscale* 9 (2017), pp. 7814–7821. DOI: 10.1039/c6nr08069c.

[10] J. Halverson, J. Smrek, and K. Kremer. "From a melt of rings to chromosome territories: the role of topological constraints in genome folding". In: *Reports on Progress in Physics* 77 (2014), p. 022601. DOI: 10.1088/0034-4885/77/2/022601.

[11] P. Sharma. "Self-Assembly of Colloidal Particles". In: *Resonance* 23 (2016), pp. 263–275. DOI: 10.1007/s12045-018-0616-0.

[12] M. Rinaldin et al. "Colloid supported lipid bilayers for self-assembly". In: *Soft Matter* 15 (2019), pp. 1345–1360. DOI: 10.1039/c8sm01661e.

[13] Yong Wang et al. "Shape-controlled synthesis of hollow silica colloids". In: *Langmuir* 29 (2013), pp. 11575–11581. DOI: 10.1021/la402769u.

[14] B. Midtvedt, J. Pineda, and G. Volpe. "Quantitative digital microscopy with deep learning". In: *Applied Physics Reviews* 8 (2021), p. 01131. DOI: 10.1063/5.0034891.

[15] S. Helgadottir, A. Argun, and G. Volpe. "Digital video microscopy enhanced by deep learning". In: *Optica* 6 (2019), p. 506. DOI: 10.1364/optica.6.000506.

[16] L. Rossi, V. Soni, and W. Irvine. "Shape-sensitive crystallization in colloidal superball fluids". In: *Proceedings of the National Academy of Sciences* 112 (2015), pp. 5286–5290. DOI: 10.1073/pnas.1415467112.

[17] *Trackpy: Fast, Flexible Particle-Tracking Toolkit*. 2021. URL: http://soft-matter.github.io/trackpy/v0.5.0/.

[18] *clustertracking 1.0 documentation*. 2021. URL: https://caspervdw.github.io/clustertracking/.

[19] J. Crocker and D. Grier. "Methods of Digital Video Microscopy for Colloidal Studies". In: *Journal of Colloid and Interface Science* 179 (1996), pp. 298–310. DOI: 10.1006/jcis.1996.0217..

[20] L. Rossia, S. Sacanna, and W. Irvine. "Cubic crystals from cubic colloids". In: *Soft Matter* 7 (2011), pp. 4139–4142. DOI: 10.1039/c0sm01246g.

[21] S. Henkes, C. Brito, and O. Dauchot. "Extracting vibrational modes from fluctuations: a pedagogical discussion". In: *Soft Matter* 8 (2021), p. 6092. DOI: 10.1039/c2sm07445a.